Mesoscale Structures of Two Comma Cloud Systems over the Pacific Ocean

STEVEN BUSINGER AND PETER V. HOBBS

Department of Atmospheric Sciences, University of Washington, Seattle, WA 98195

(Manuscript received 8 May 1986, in final form 9 February 1987)

ABSTRACT

Satellite and synoptic data are used to establish the environments in which two comma cloud systems occurred over the Pacific Ocean; serial rawinsonde, aircraft, and single- and dual-Doppler radar data provide information on the mesoscale and microscale structures of the systems.

The disturbances formed within polar air masses in regions of moderately strong cyclonic vorticity. A surface low-pressure center was associated with the comma cloud, and a surface-pressure trough was situated under the tail of the comma cloud. In both cases, there was a wind maximum near 850 mb, located on the southeast flank of the comma cloud, just ahead of the short-wave trough.

Well-defined rainbands were present in both comma cloud systems. The average width of the rainbands was ~20 km and their average separation ~ 30 km. The rainbands were aligned along the direction of the mean wind and perpendicular to the thermal wind over the depth of the rainbands. Precipitation cores, produced by embedded convection, within the rainbands had an average spacing along the length of the rainbands of ~17 km. The precipitation cores contained updraft speeds of several meters per second and relatively high liquid water contents; they retained their identities over periods of several hours. Wind shifts, lines of convergence and associated updrafts occurred at low levels toward the rear of the rainbands. At higher levels, cloud particles moved from the rear toward the front of the rainbands, where they fell out as precipitation through a low-level flow of moist air. The precipitation was augmented by convective elements in an unstable layer near the top of the rainband, which produced ice crystals that grew by riming and aggregation as they fell through the low-level, moist inflow.

The spacing and orientation of the rainbands can be explained by the theory for mixed dynamic/convective instability developed by Sun. The precipitation cores embedded in the rainbands may have been the result of enhanced updrafts at the points where inflection-point instability rolls, oriented nearly perpendicular to the length of the rainbands, intersected the rainbands.

1. Introduction

Since the advent of the meteorological satellite imagery, it has become apparent that a profusion of cyclonic vortices occur in polar airmasses behind or poleward of the polar front (Anderson et al., 1969; World Meteorological Organization, 1973). These vortices span a continuum of sizes, ranging from a few hundred kilometers to >1000 km in diameter, and a wide range of intensities, from light breezes to hurricane force winds (Reed, 1979; Locatelli et al., 1982; Mayengon, 1983; Rasmussen, 1983; Forbes and Lottes, 1985).

Cyclonic vortices in polar airmasses have been separated into two broad categories, corresponding to two perceived extremes in the spectrum of disturbances (Rasmussen, 1981, 1983; Businger, 1985; Reed and Blier, 1986a,b). At the smaller end of the spectrum is the "*polar low*" (sometimes referred to as the "*arctic instability low*"). Polar lows, which appear as spiral-shaped cloud patterns on satellite images, form at high latitudes, under closed, cold-core lows at 500 mb, during outbreaks of arctic air (Rasmussen, 1979, 1981, 1983, 1985; Wilhelmsen, 1981; Businger, 1985). At the larger end of the spectrum is the *comma cloud system* (*comma cloud*, for short), which can range from a large mesoscale to a small synoptic-scale feature that develops in regions of enhanced tropospheric baroclinicity, often near preexisting frontal boundaries. The term comma cloud is an abbreviation of "comma-shaped cloud pattern", and was introduced to denote a characteristic cloud signature seen in cold airmasses. Reed (1979) noted that a region of enhanced convection precedes the formation of comma clouds. Conditions associated with this enhancement include differential positive-vorticity advection and conditionally unstable lapse rates. Since a continuous spectrum of disturbances exist in polar airmasses, it is not always easy to fit cyclonic vortices into polar lows or comma clouds.

The subsynoptic scale of cyclonic vortices, and their rapid development, typically over data-sparse oceans, has made it difficult to obtain good observational data. It has also contributed to the challenge of synthesizing coherent physical models to describe their dynamics and growth, and to the difficulties in forecasting their development and movement.

Only two previous studies have examined the mesoscale structures of comma clouds. Harrold and

Browning (1969) studied a polar low[1] that produced heavy snowfalls over Britain and concluded that the disturbance was primarily baroclinic in nature. Although comma clouds are generally considered to be nonfrontal disturbances, Locatelli et al. (1982) found that comma clouds, in their mature stages at least, can develop advection and mesoscale precipitation patterns that are indistinguishable from those associated with the fronts of larger midlatitude cyclones, as summarized by Hobbs (1978).

In this paper, we describe the synoptic, mesoscale and microscale structures of two comma clouds as they crossed the Pacific Coast of Washington State. We then discuss the microphysical processes that produced the precipitation and the mechanisms that might have been responsible for the mesoscale organization of the precipitation within the two systems.

2. Data sources

On 17 January 1982 and 10 February 1982, cyclonic vortices crossed the Washington Coast. Since the vortices formed within polar airmasses were on the small synoptic scale (~1000–1500 km wavelengths), and were nonfrontal in origin, they are classified as comma clouds. Figures 1a, b show the geostationary satellite imagery for both cases as the storms neared the Washington Coast. The tail of the comma cloud is visible over the water to the west of Washington. The *CY*-*CL*onic *E*xtratropical *S*torms (CYCLES) observational network (Hobbs et al., 1980) on the Washington Coast provided an opportunity to investigate the mesoscale structures and precipitation-producing mechanisms associated with these comma clouds. These topics are the primary focus of this paper.

The data that will be used to describe the mesoscale structures of the two comma clouds come from two 5.45 cm wavelength scanning Doppler radars, an 8.6 mm wavelength vertically pointing Doppler radar, serial rawinsondes, and standard meteorological measurements from a number of special ground stations in western Washington. One of the scanning Doppler radars, the vertically pointing Doppler radar, and the radiosonde unit were located at Pt. Brown, on the Washington Coast. The other scanning Doppler radar was located on the coast at Oysterville, 42 km south of Pt. Brown. Cloud microphysical measurements in the two comma clouds were provided by the University of Washington's B-23 research aircraft (Hobbs et al., 1980), and a NOAA P-3 research aircraft. Synoptic data were available from the regular surface network, ship and buoy reports, and satellite imagery.

[1] Based on the definitions given above, the system referred to as a polar low by Harrold and Browning would better be termed a comma cloud.

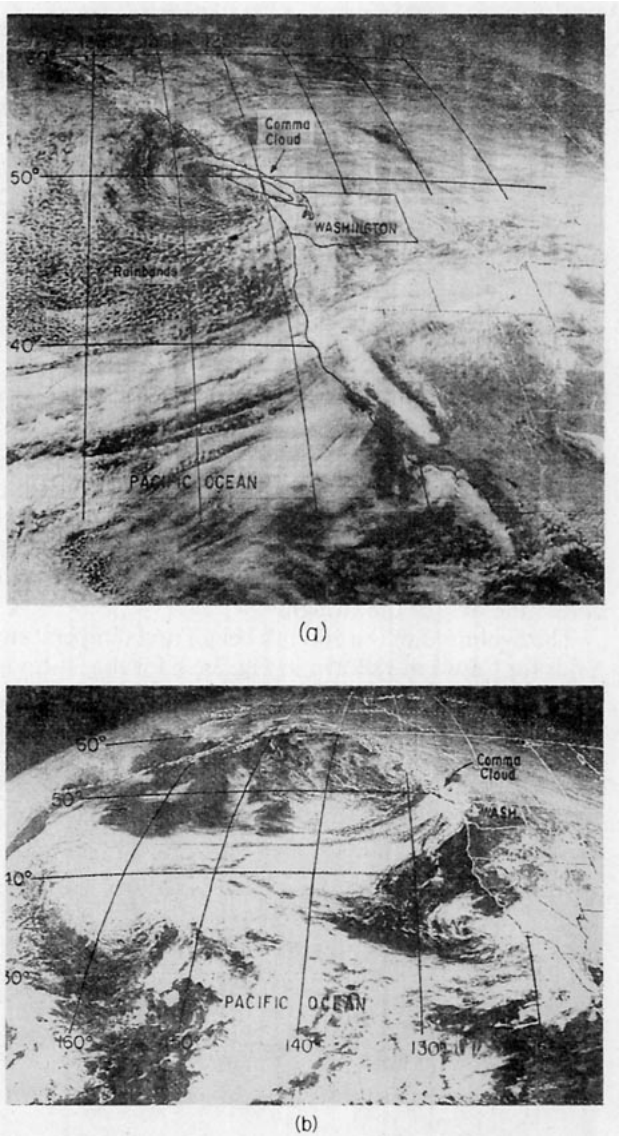

FIG. 1. Geostationary-satellite images (visible) of the two comma clouds described in this paper. (a) Case 1: 1115 PST 17 January 1982 and (b) Case 2: 1415 PST 10 February 1982.

3. Synoptic overview of the comma clouds

There were no special synoptic-scale observations made on 17 January or 10 February 1982. Therefore, only a brief summary of the synoptic-scale events leading up to the formation of the comma clouds will be given here. The upper-level maps presented in this section are the NMC final analyses; surface maps were reanalyzed incorporating all of the available ship data.

a. Case 1

A pair of comma clouds developed in the wake of an occluded front that passed onto the Washington Coast on 16 January 1982 (the occlusion has been de-

scribed by Wang and Hobbs, 1983). Figure 2a shows a comma cloud approaching the Washington Coast, and a second incipient comma cloud developing out of a region of high clouds to the northwest of the first comma cloud. The comma clouds developed from small areas of high cloud that migrated from the leading edge of a synoptic-scale trough along the cloud band of the occlusion, to the trailing side of the trough. The second of these two comma clouds is analyzed in this paper.

In satellite imagery, these two comma clouds over the Pacific Ocean appear similar to those that form over the Atlantic Ocean (Zick, 1983). Using winds derived from geostationary satellite imagery, Zick showed that comma clouds over the Atlantic form from preexisting vorticity centers that migrate from the front side to the rear side of large-scale troughs. The schematic in Fig. 2b depicts the evolution of the cloud shield associated with a developing comma cloud as the latter moves down the trailing side of a 500 mb trough and across the axis of the trough.

The evolution of the 500 mb height and temperature fields for Case 1 are shown in Fig. 3a, b for the 24-hour period starting at 1600 PST 16 January. Figure 3c shows the 850 mb height and temperature fields at 1600 PST on 16 January. The two comma clouds were both located along the poleward edge of a large-scale jet stream in the middle and upper troposphere, in a region of moderately strong cyclonic shear and baroclinicity. The positions of the short-wave troughs associated with the comma clouds, as deduced from surface observations and satellite photographs, are shown in Fig. 3. Upper-level support for the trailing comma cloud deteriorated as it reached the Washington Coast (Fig. 3b).

The evolution of the surface-pressure field and pressure tendencies for Case 1 are shown in Fig. 4. The domain of the surface pressure maps has been reduced from that in Fig. 3 to document the small synoptic-scale features of the disturbance. The surface low-pressure center was associated with the comma cloud, and a pressure trough extended under the comma tail.

b. Case 2

The synoptic environment of the other comma cloud to be analyzed here differed from that of Case 1 in that a high-amplitude, blocking ridge dominated the eastern Pacific Ocean at the 500 mb level on 9 February 1982. A short-wave trough passed over the crest of the ridge and gradually deepened as it moved down the leading edge of the ridge on 10 February (Fig. 5). The formation of a comma cloud accompanied this development. The tail of the comma cloud is visible west of Washington in Fig. 1b. Figure 5a–c show the evolution of the 500 mb height and temperature fields at 24 hour intervals, starting at 1600 PST 8 February. Figure 5d shows the

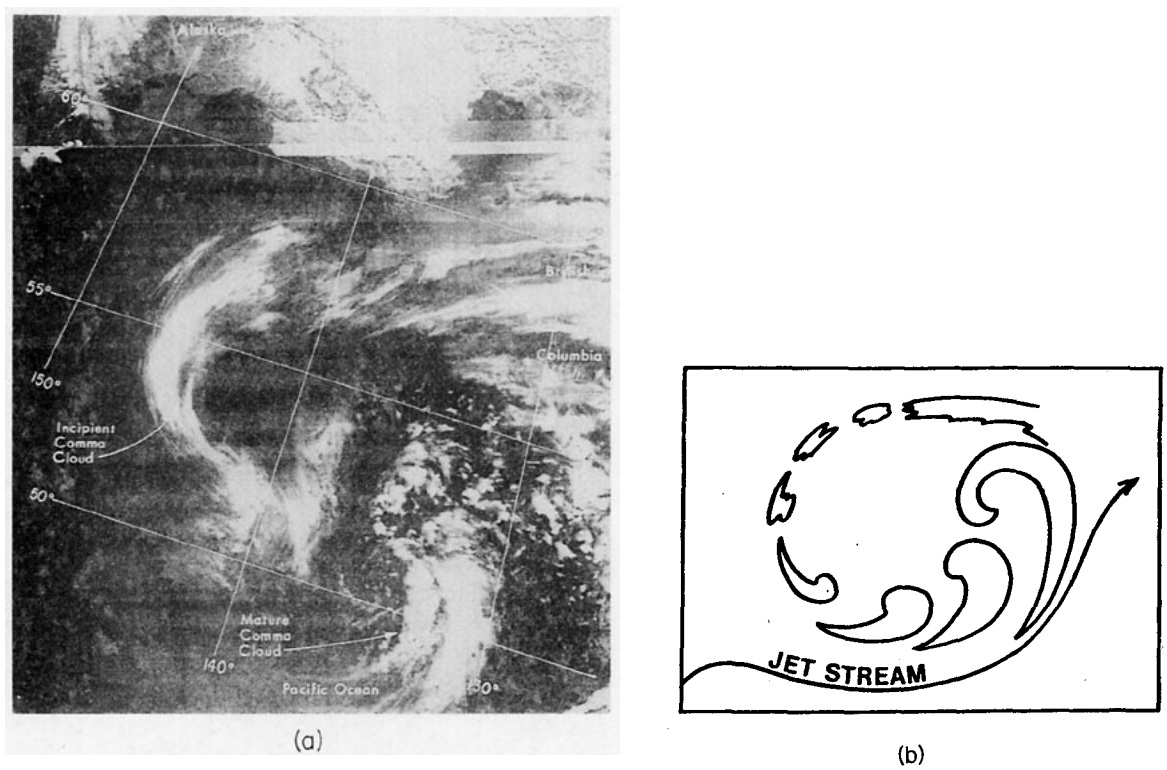

FIG. 2. (a) NOAA-7 infrared-satellite image at 1508 PST 16 January 1982, showing high clouds associated with the incipient comma cloud for Case 1 (upper left) and a mature comma cloud (lower right). (b) Schematic depiction of the principle life cycle of a comma cloud from the incipient stage to the mature vortex (from Zick, 1983).

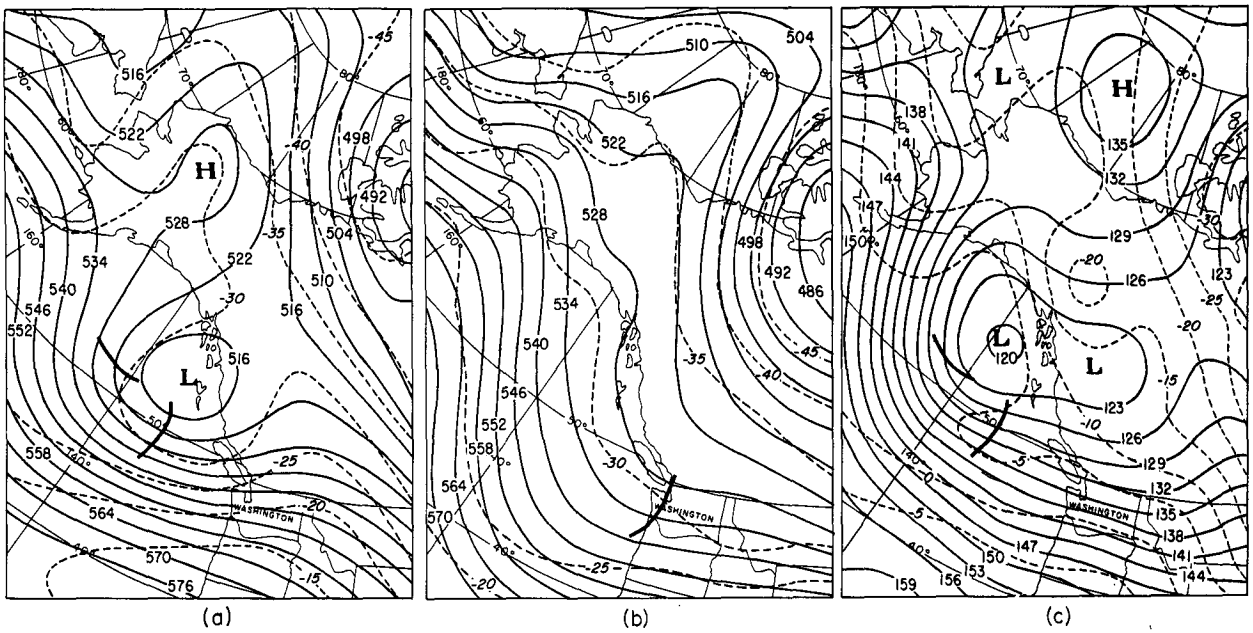

FIG. 3. Geopotential heights (continuous lines, labeled in tens of meters) and temperatures (dashed lines, labeled in °C) for (a) 500 mb at 1600 PST on 16 January 1982, (b) 500 mb at 1600 PST 17 January 1982, and (c) 850 mb at 1600 PST 16 January 1982. The heavy lines show the position of the short-wave troughs associated with the comma clouds.

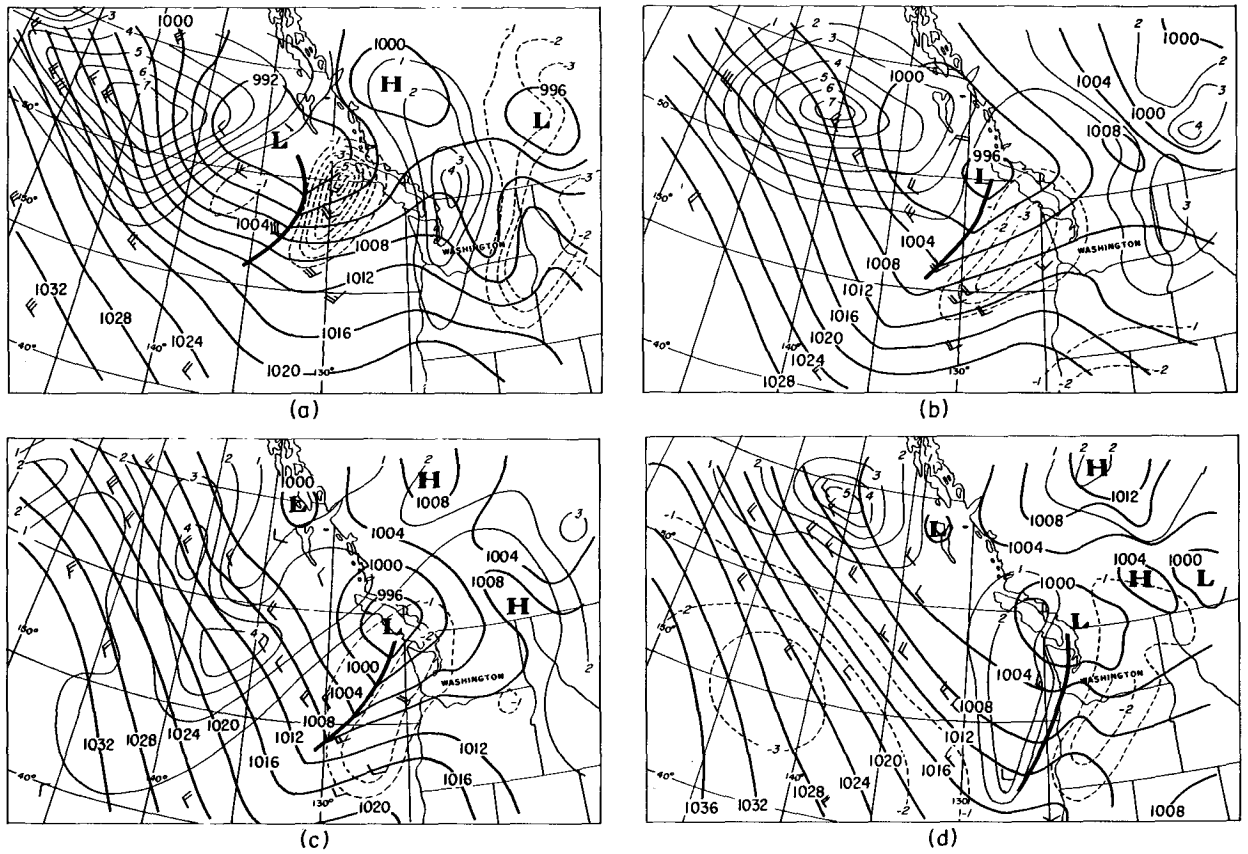

FIG. 4. Evolution of the surface-pressure field for Case 1. Heavy contours are surface pressure every 4 mb, light and dashed contours are the rising and falling pressure tendencies (in mb/6 h), respectively. (a) 2200 PST 16 January 1982, (b) 0400 PST 17 January 1982, (c) 1000 PST 17 January 1982 and (d) 1600 PST 17 January 1982.

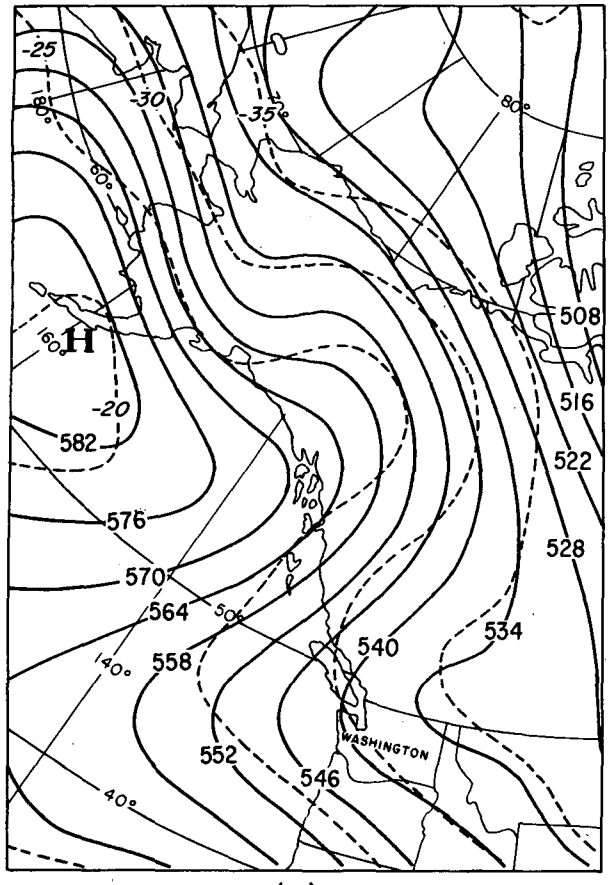
H
-25
-30
-35
-20
582
576
570
564
558
552
546
540
534
528
522
516
508
WASHINGTON

(a)

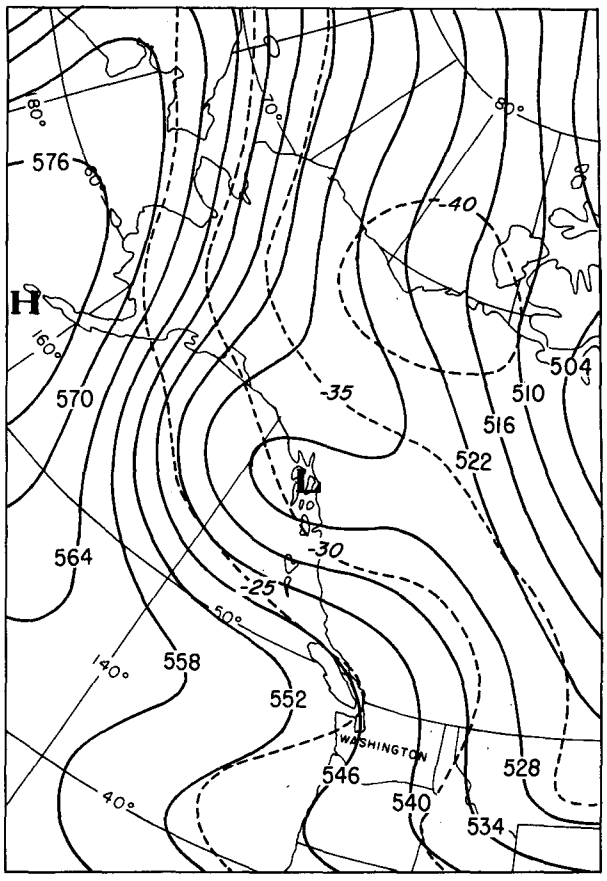
H
576
570
564
558
552
546
540
534
528
522
516
510
504
-40
-35
-30
-25
WASHINGTON

(b)

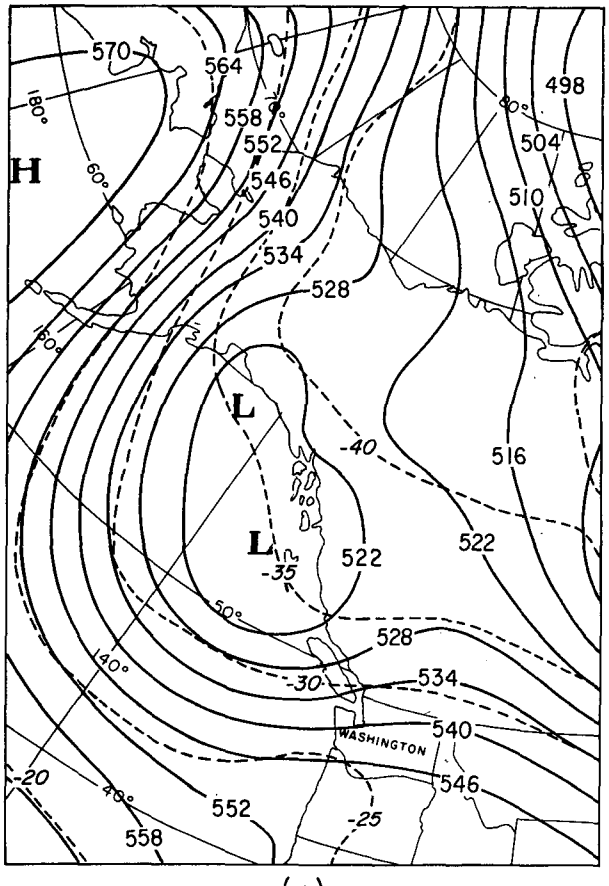
H
L
L
570
564
558
552
546
540
534
528
522
516
510
504
498
-40
-35
-30
-25
-20
WASHINGTON

(c)

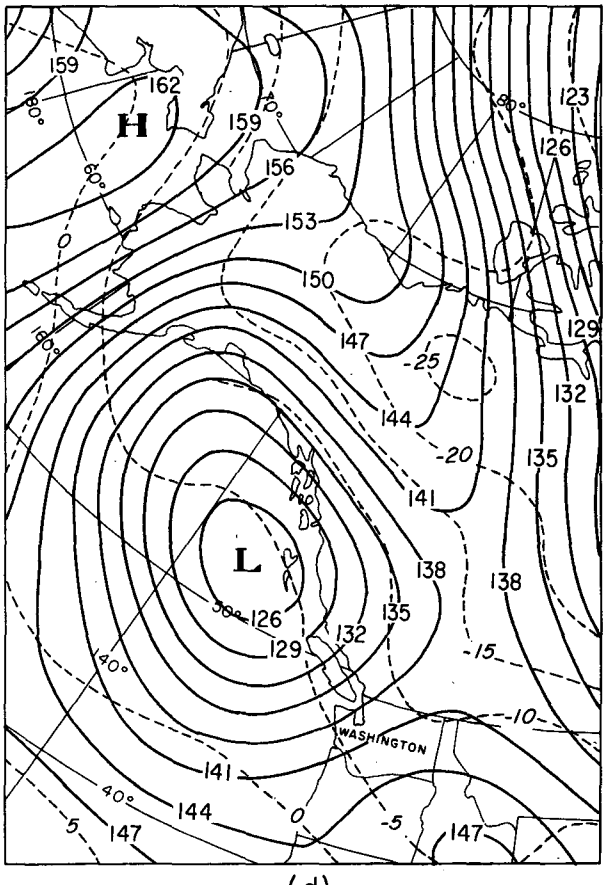
H
L
159
162
159
156
153
150
147
144
141
138
135
132
129
126
123
-25
-20
-15
-10
-5
0
5
WASHINGTON

(d)

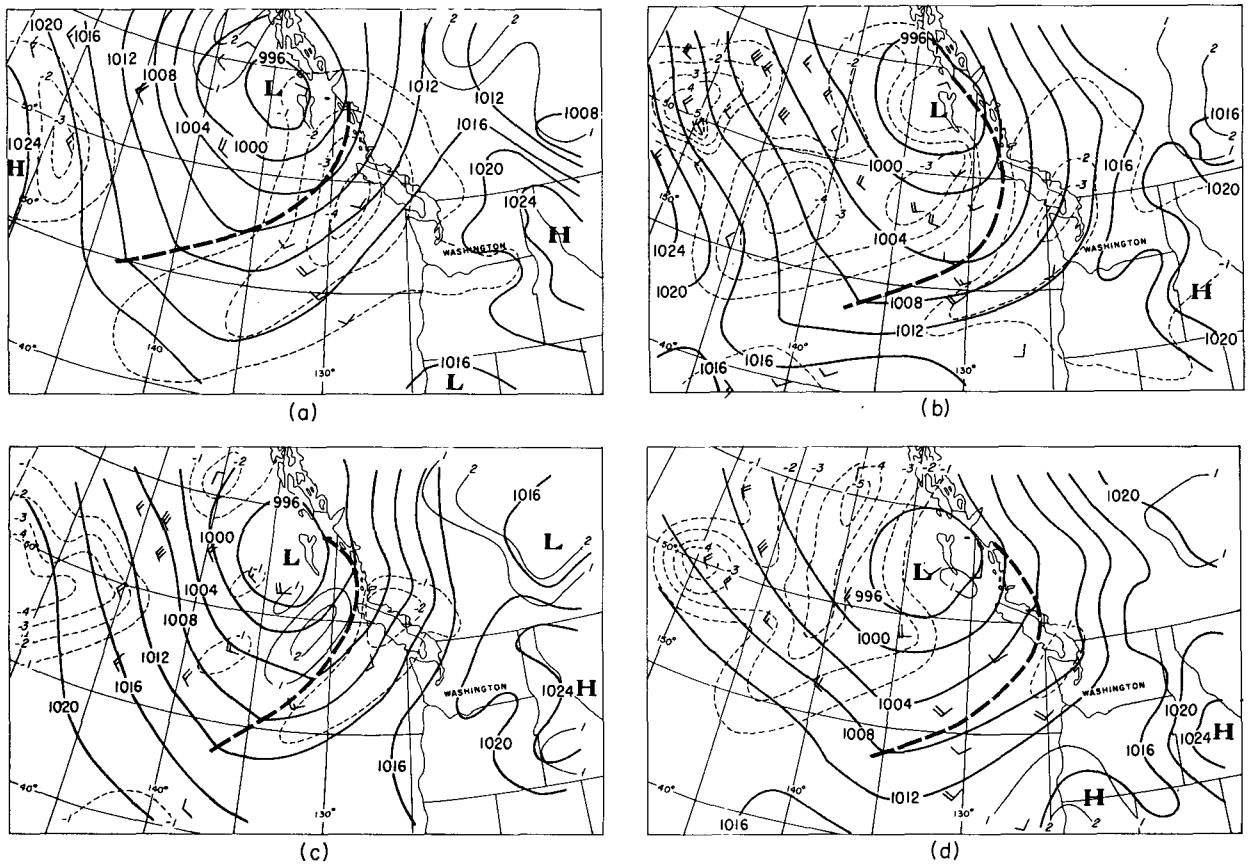

FIG. 6. Evolution of the surface-pressure field for Case 2. Heavy contours are surface pressure every 4 mb, light and dashed contours are the rising and falling pressure tendencies (in mb/6 h), respectively. (a) 0400 PST 10 February 1982, (b) 1000 PST 10 February 1982, (c) 1600 PST 10 February 1982 and (d) 2200 PST 10 February 1982.

850 mb height and temperature fields for 1600 PST 10 February.

Calculations from the geopotential height field showed that a positive vorticity maximum was associated with the short-wave trough. When this trough reached the inflection point between the ridge and the trough, it grew rapidly at 500 mb during the 24 h period starting at 1600 PST 9 February. Similar increases in scale of developing disturbances have been documented in comma clouds west of California by Reed and Blier (1986a,b). As the comma cloud neared the Washington Coast, the thermal support deteriorated and only weak warm advection was evident at 850 mb at 1600 PST 10 February (Fig. 5d). Consequently, the surface low-pressure center began to weaken.

Figure 6 shows the evolution of the surface-pressure field and the pressure tendencies at 6 h intervals starting at 0400 PST 10 February. Again, a low-pressure center was present at the surface, while a trough axis lay under the comma tail.

4. Vertical cross sections of temperature and wind

a. Case 1

Shown in Fig. 7 are time–height cross sections[2] of temperature and wind for Case 1. (In Fig. 7, the time scale on the right-hand side of the abscissa has been foreshortened to reduce the width of the figure.) The temperature contours in Fig. 7a show cooling in the atmosphere below 5 km from 1000 to 1400 PST 17

[2] Since the comma clouds were mature when they reached the Washington coast, we have assumed that they were in steady state, so that a time-to-distance transformation can be used to create cross sections. This assumption should be kept in mind when interpreting the cross sections.

FIG. 5. Geopotential heights (continuous lines, labeled in tens of meters) and temperatures (dashed lines, labeled in °C) for (a) 500 mb at 1600 PST on 8 February 1982, (b) 500 mb at 1600 PST on 9 February 1982, (c) 500 mb at 1600 PST on 10 February 1982 and (d) 850 mb at 1600 PST on 10 February 1982.

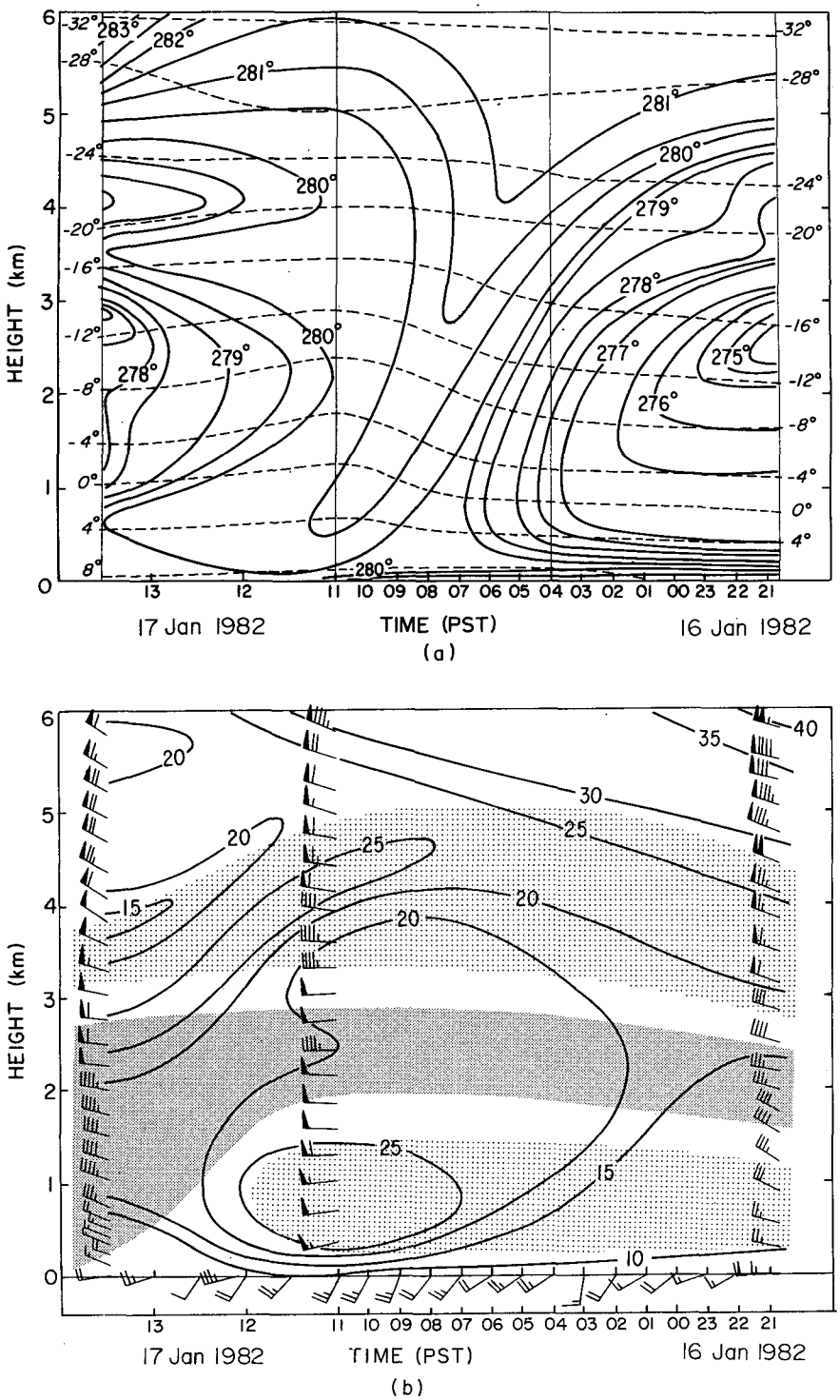

FIG. 7. Time-height cross section for Case 1 (16–17 January 1982) based on radiosondes launched at Pt. Brown: (a) temperature (°C)—dashed contours, wet-bulb potential temperature (°K)—solid contours. Thin vertical lines indicate the times of rawinsonde launches. (b) Contours of wind speed (in m s^{-1}) parallel to the orientation of rainbands. The actual wind speed and directions are shown by the wind barbs (flag: 25 m s^{-1}, barb: 5 m s^{-1}). In (b) areas of continuous shading indicate backing of the wind with height, and areas of speckled shading indicate veering of the wind with height.

January. The wet-bulb potential temperature contours reveal more structure, with a tongue of warm, moist air just preceding the surface-pressure trough and colder, drier air moving in behind the trough.

The wind speed reached a peak in excess of 25 m s^{-1} in the lower troposphere near 850 mb on the southeast flank of the comma cloud, just ahead of the surface pressure trough (Fig. 7b). This feature is characteristic of most of the case studies of polar vortices that have been described in the literature (e.g., Harrold and Browning, 1969; Reed, 1979; Locatelli et al., 1982); it is consistent with the presence of a tongue of warm air ahead of the trough and thermal wind balance. Also depicted in Fig. 7b are the regions of warm- and cold-air advection (veering/backing of the wind). Warm advection dominated the forward edge of the comma cloud and cold advection the rear edge, especially below 700 mb, thus maintaining low-level baroclinicity in the storm.

b. *Case 2*

A time–height section of temperature for Case 2 is shown in Fig. 8a. The dashed temperature contours show very little change with time, reflecting the fact that the vortex was dissipating as it neared the Washington Coast. The wet-bulb potential temperature contours, however, reveal a great deal of structure. A layer of moist potential instability near 2 km (on the right-hand side of Fig. 8a), gradually increased in height with time to about 3.5 km by 1800 PST 10 February. The shaded area in Fig. 8a indicates a region of precipitating cloud (deduced from the radar measurements). We will show below that small convective elements originated in this zone of instability, and that enhanced concentrations of ice particles emanated from this layer and grew by riming and aggregation in the lower layers of the rainband, thereby enhancing precipitation.

Wind data for Case 2 are shown in Fig. 8b. As in Case 1, the wind speed reached a maximum near 850 mb on the southeast flank of the comma cloud. However, in Case 2, the lower troposphere was dominated by warm-air advection for the entire period (light shaded region in Fig. 8b), with a thin layer of cold-air advection above. West to northwest winds in this layer brought cool, dry air from the northern Gulf of Alaska over warmer moist air from the southwest, resulting in potential instability (Fig. 8a).

5. Organization of the precipitation

The distrubution of precipitation in the two comma clouds were analyzed using 0° PPI scans from the radar located at Pt. Brown. In both cases, there were well-defined rainbands, with embedded cores of higher precipitation.

a. *Case 1*

Shown in Fig. 9 are six rainbands in the comma cloud of Case 1. Using the 10 dBZ reflectivity contour as a boundary, the average spacing between the rainbands was ~30 km and their average width ~20 km, corresponding to a wavelength[3] of ~50 km. The largest of the rainbands, numbered 4 in Fig. 9, had the strongest wind shift and highest radar reflectivity. The motions of some of the rainbands are displayed in Fig. 10. The precipitation cores [>25 dBZ] embedded within the rainbands retained their identities and strengths over periods of several hours (e.g., see Fig. 10b).

Table 1 summarizes the speeds and directions of motion of the rainbands and the precipitation cores. The speed of a rainband is defined as its component of motion perpendicular to its length. The direction of motion of the rainbands and the precipitation cores gradually shifted clockwise as subsequent rainbands moved on to the coast (Table 1). At the same time, the wind shear over the depth of the rainbands gradually turned clockwise, to a more northwesterly direction, as the trough axis of the comma cloud passed Pt. Brown. To the extent that the winds were in thermal wind balance, the wind shear can be approximated by the thermal wind. Thus, as the thermal wind vector over the depth of the rainbands rotated clockwise, the rainbands also rotated clockwise, with their lengths remaining oriented approximately perpendicular to the thermal wind.

The steering level for the precipitation cores was in the boundary layer, at a height of ~0.5 km. The core velocities correlated well with peak surface gusts measured by buoy. Hence, core velocities might be a useful aid in deducing surface winds. The radar reflectivity data showed that the precipitation cores were shallow, with regions > 30 dBZ generally below 1.5 km. The precipitation cores moved slightly slower than the wind along the length of the rainbands below 1.5 km.

Shown in Fig. 11 is a vertical cross section of the radar reflectivity pattern across the width of the rainband, numbered 4 in Fig. 9. The pattern shows small, vertically oriented cores of higher reflectivity near the forward edge of the rainband, with a broader region of higher reflectivity toward the rear of the rainband. The sharp decrease in reflectivity at the rear of the rainband was located just behind an abrupt shift in the wind direction at the surface, which was evident on the 0° Doppler-velocity patterns for this time period.

b. *Case 2*

A series of rainbands was also associated with the comma cloud of Case 2. Two of the stronger rainbands

[3] The wavelength is the distance from the middle of one rainband to the middle of the next.

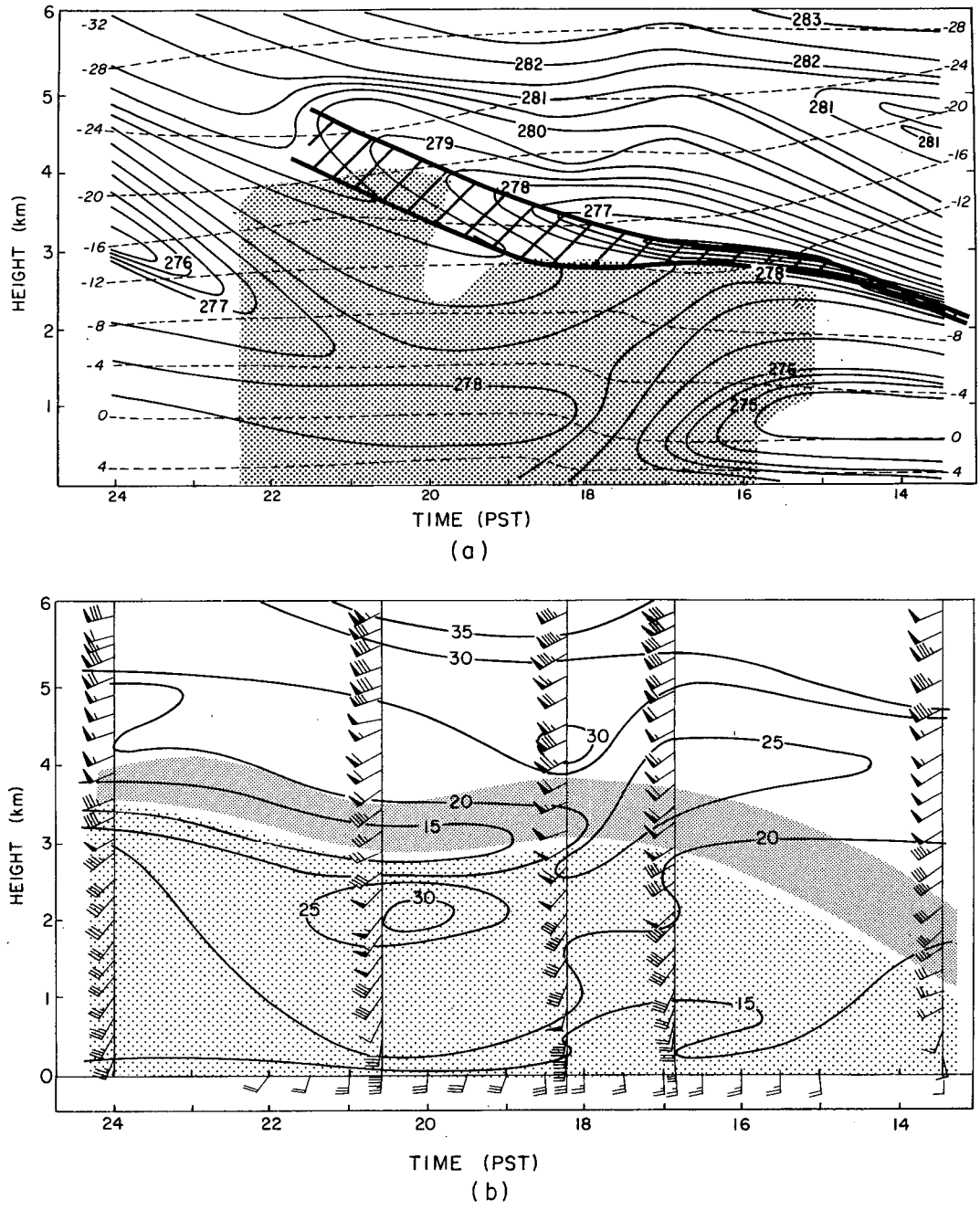

FIG. 8. As in Fig. 7 but for Case 2 10 February 1982. In (a) the shading indicates the extent of the precipitation echo detected by the vertically-pointing radar, and the hatched area outlined with heavy lines shows the region where the wet-bulb potential temperature decreased with height.

can be seen in the radar reflectivity pattern shown in Fig. 12. The first rainband (numbered 1) appeared as a region ~40 km wide of stratiform precipitation, although it contained some embedded cores.

Reflectivity data, taken by the vertically pointing Doppler radar in a region of rainband 1 that was devoid of large precipitation cores, shows a low layer of stratiform precipitation, extending to a height of ~1.5 km, with a series of small, embedded convective cells extending to about 3 km (Fig. 13). Fallstreaks, emanating from the upper-level cells, enhanced the precipitation in this rainband. Comparison of the thermal data (Fig.

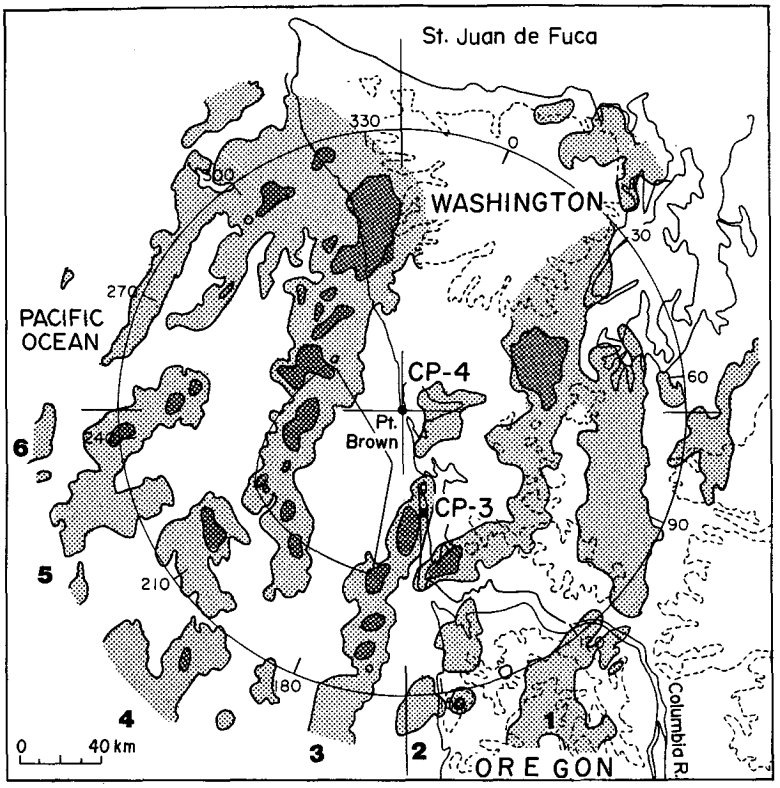

FIG. 9. Radar reflectivities for Case 1 at 1033 PST 17 January 1982. Light shading is ≥10 dbZ and dark shading is ≥25 dBZ. The large circle shows the 120 km radar range centered at Pt. Brown. Six rainbands (numbered 1–6) were present.

8a) with the vertically pointing radar data, shows that the convective cells formed in a layer that was unstable to moist ascent (i.e., in a region where the wet-bulb potential temperature decreased with height). The wind direction at the mean height of the convective cells matches that of the precipitation cores. However, the speed of the cores was much less than that of the cells, due probably to the fact that the cores were produced by low-level convergence in the planetary boundary layer.

Rainband 2 in Case 2 was only ~25 km wide and it contained precipitation cores as it passed over Pt. Brown, with radar echoes that extended from the boundary layer to nearly 4 km. Small convective cells at upper levels, similar to those observed in rainband 1, were present ahead of the deeper convective core. The rise in the height of the radar echoes coincided with a rise in the level of the layer of moist potential instability (Fig. 8a).

The velocities of the rainbands and precipitation cores in rainband 2 were similar to those in rainband 1. The rainband velocity was ~2.3 m s^{-1} from 293°, and the core velocity ~ 8.2 m s^{-1} from 225°. The speed and direction of the precipitation cores corresponded to a steering level in the boundary layer below 0.5 km (as in Case 1), and the main radar echoes were confined below ~1.5 km.

6. Airflow in the rainbands

a. Case 1

Dual-Doppler radar data were not available for Case 1. Therefore, single-Doppler radar measurements from Pt. Brown were used to deduce the airflow patterns in the rainbands of Case 1, under the assumption that variations in the airflow parallel to the rainbands was small compared to that across the rainbands.

Shown in Fig. 14 is the derived airflow (relative to the rainband) for a portion of rainband 4 of Case 1. The radar-reflectivity pattern showed variations along the band (Fig. 12), therefore, caution should be exercised in interpreting the airflow shown in Fig. 14. Velocity data from the Doppler radar indicated a well-defined wind shift line 68 km west of Pt. Brown at the time of the airflow in Fig. 14. This wind shift occurred near the rear edge of rainband 4, and was the strongest wind shift observed in the storm. It can be seen from this figure that there was significant convergence and upward motion associated with the wind shift line with

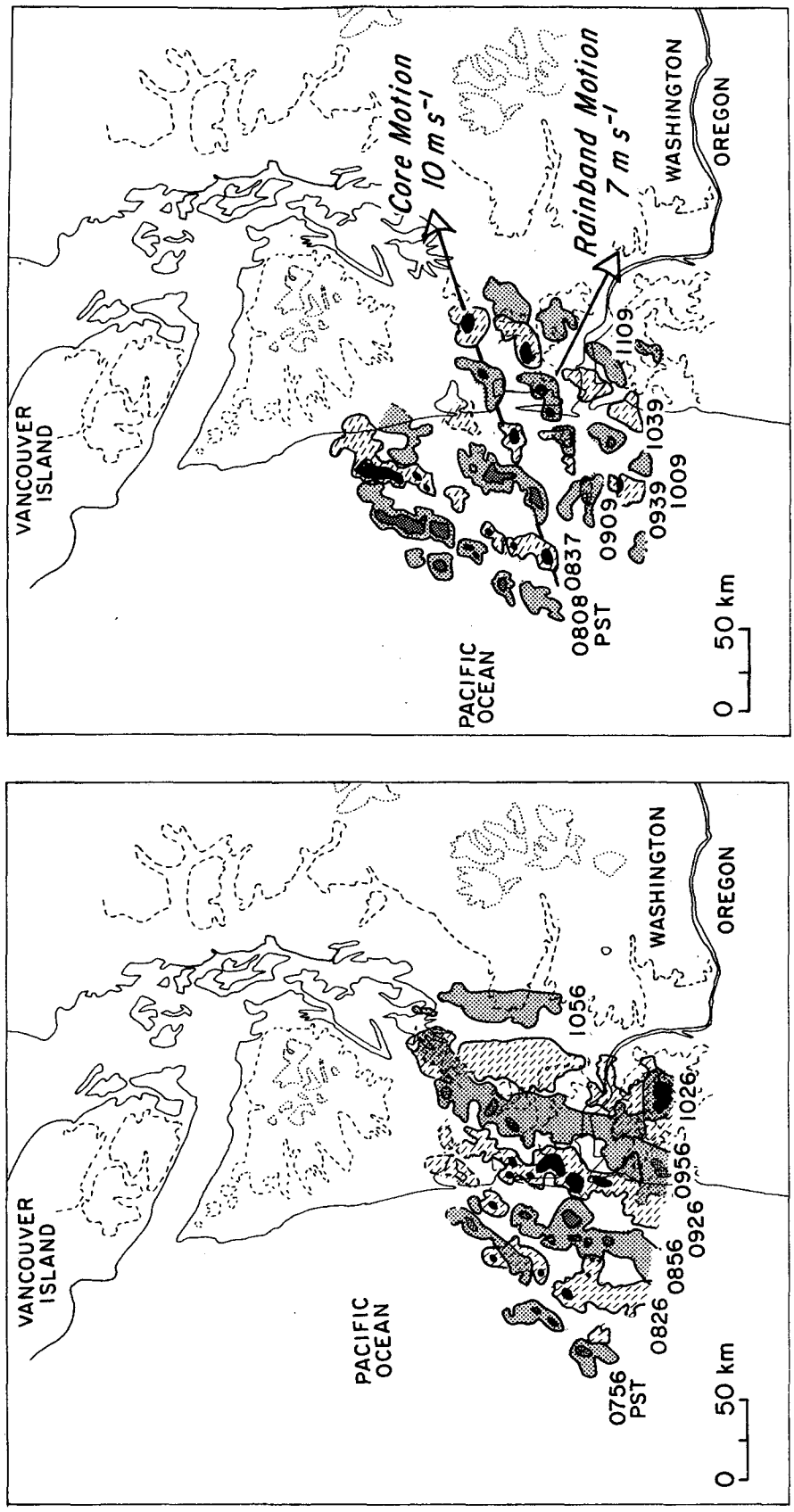

FIG. 10. The locations at various times of rainbands 2, 3, 4 and 5 in Case 1 are shown in (a)–(d), respectively. Rainband and core motions are indicated by the arrows in (b).

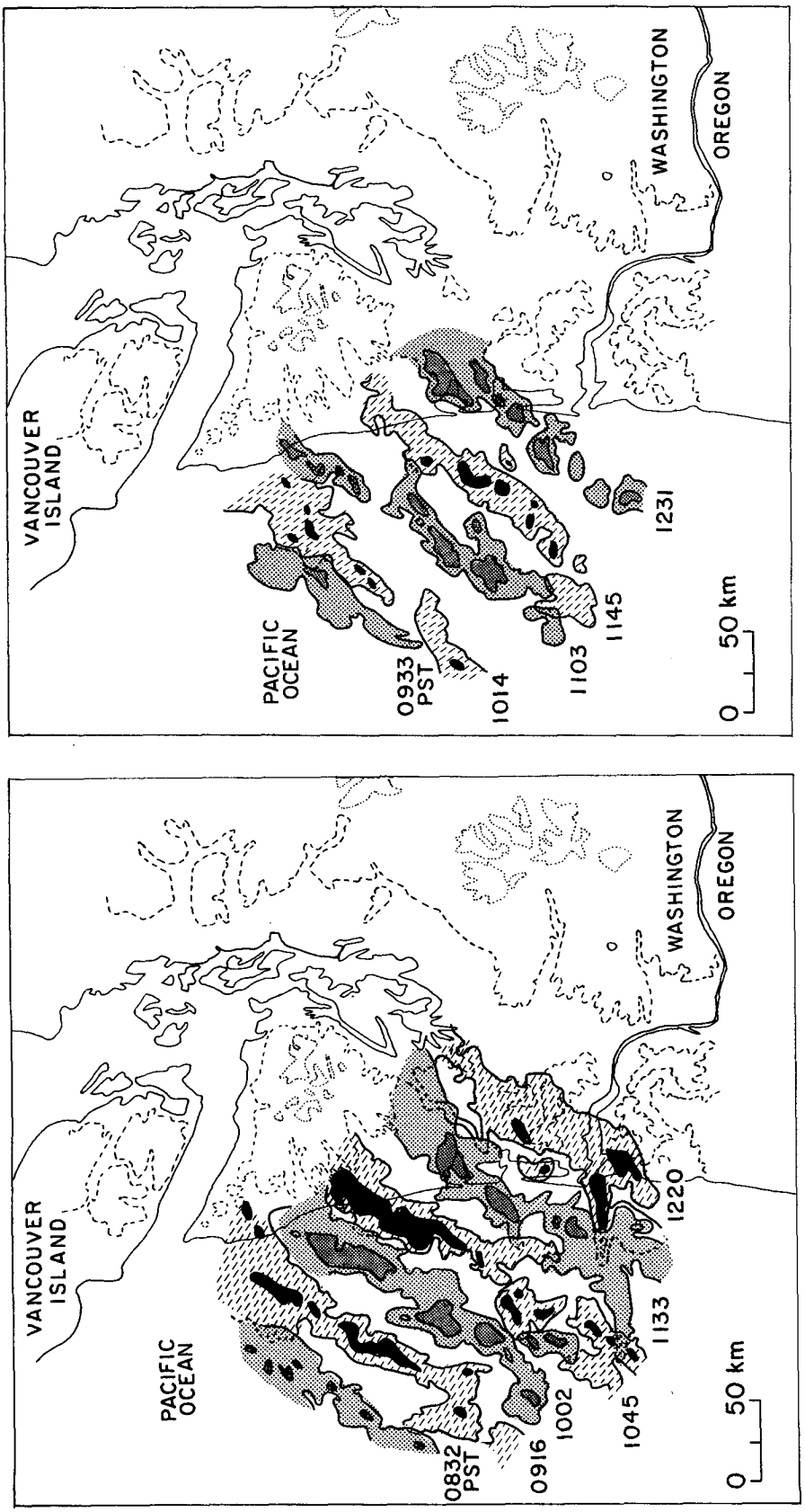

FIG. 10. (*Continued*)

TABLE 1. Speeds and directions of motion of the rainbands and precipitation cores in the comma cloud of 17 January 1982 (Case 1).

Rainband number (see Fig. 9)	Rainband speed (m s^{-1})	Direction of motion of rainband (from, in deg)	Speed of precipitation cores (m s^{-1})	Direction of motion of precipitation cores (from, in deg)
1	7.0	293	10.8	245
2	7.7	291	10.1	247
3	7.2	293	10.3	247
4	7.6	296	11.0	247
5	8.5	303	11.6	255
6	8.1	301	9.0	270

relative inflow from the east at low levels ahead of the convergence; at higher levels and toward the rear of the band the relative flow was from the west.

b. Case 2

Three-dimensional airflow fields were derived from dual-Doppler radar data for three of the rainbands in Case 2. Doppler velocity and reflectivity data were taken in the form of simultaneous coplanes at each of the two radars. The data were processed to remove interferences from ground clutter and sidelobes and then filtered, using a Cressman scheme with a 500 m radius of influence in the horizontal and 300 m in the vertical. The two filtered-planar arrays of data were then integrated into a three-dimensional Cartesian grid, with 500 m horizontal and 300 m vertical grid spacing. The approximate area over which dual-Doppler data was available is indicated in Fig. 12. Horizontal and vertical cross sections of radar-reflectivity and velocity data, as well as other computed fields, such as vertical velocity and vorticity, could be derived within this area. On the scale of the dual-Doppler analysis, many variations became apparent in the velocity and reflectivity data. In this section, we will document some of these variations within the rainbands.

Some horizontal cross sections through rainband 1 in Case 2 are shown in Fig. 15. The radar reflectivity pattern shows an elongated region with reflectivity values > 30 dBZ (Fig. 15a), which is indicative of convective activity, with a sharp gradient in reflectivity along the western, rear edge of the band. The streamlines (Fig. 15b) show a line of convergence at the rear of the band. There was also a mesoscale eddy that extended through several kilometers depth. The scale of the eddy and its location coincided with a local maximum in the reflectivity pattern.

The line labeled AB in Fig. 15 is perpendicular to rainband 1. Vertical cross sections through AB of the radar reflectivity data, vertical velocities, and the airflow relative to the storm are shown in Fig. 16a–c, respectively. The location of the cross section was chosen to focus on the interesting eddy feature seen in the streamlines in Fig. 15b. The flow field indicates that convergence was located near the rear of the rainband, with relative inflow from the east at low levels, becoming westerly at higher levels. Cloud particles were probably carried aloft in this updraft, and then forward in the band where they fell out through the moist inflow at lower levels. The reflectivity pattern is consistent with this interpretation, in that the higher reflectivity values are located in a broad zone forward of the updraft. The vertical velocity pattern also confirms this pattern, showing upward motion > 1.5 m s^{-1} above the region of strongest convergence near the rear of the band.

Horizontal cross sections of reflectivity, storm-relative streamlines, and vertical air velocity in rainband 2 are shown in Fig. 17a–c, respectively. The rainband consisted of two roughly parallel lines of enhanced precipitation. Embedded cores of higher precipitation, with reflectivities > 40 dBZ, indicate the presence of moderately strong convection. The storm-relative streamlines show a complicated pattern of convergence and eddies, reflecting the cellular nature and complex structure of the precipitation pattern. The vertical air velocities at the 2.7 km level (Fig. 17c) show a pattern of small updrafts that matches the corresponding reflectivity pattern (Fig. 17a) reasonably well. Peaks in the vertical velocities (~3 m s^{-1}) were in close proximity to cores of higher precipitation.

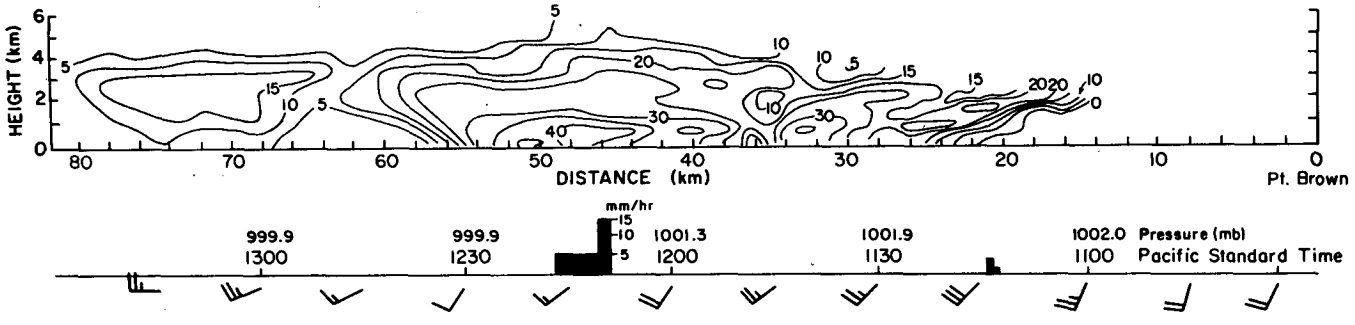

FIG. 11. Time–height cross section of the radar reflectivity (in dBZ) for rainband 4 in Case 1. Surface observations of wind and precipitation at Point Brown (time-to-distance adjusted) are also shown.

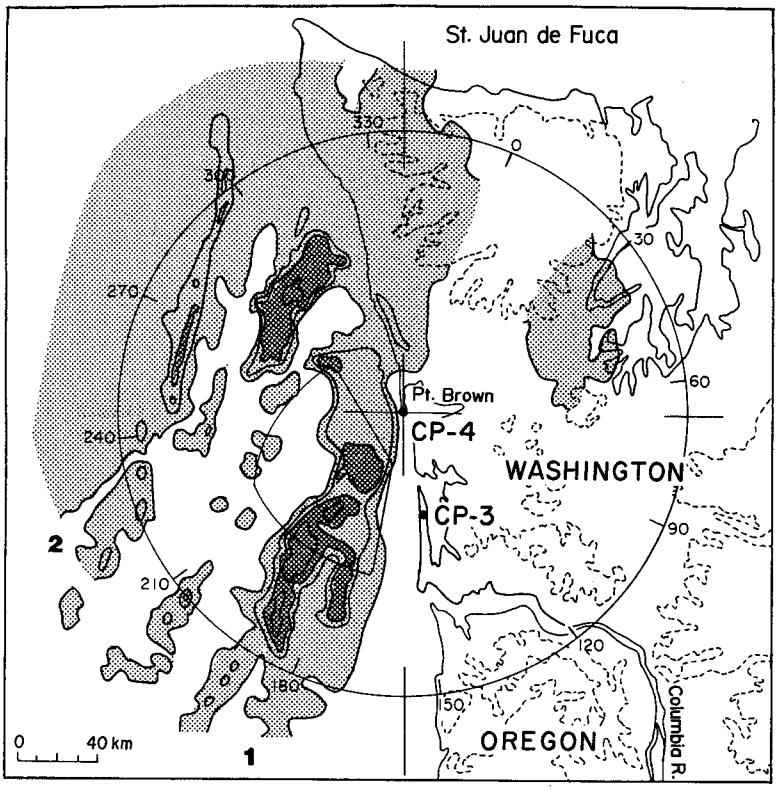

FIG. 12. Radar reflectivity at 1800 PST 10 February 1982 for Case 2. Light shading is ≥10 dBZ and dark shading is ≥25 dBZ. The roughly double triangular area that is lightly outlined just to the west of Point Brown indicates the region where dual-Doppler radar measurements were obtained.

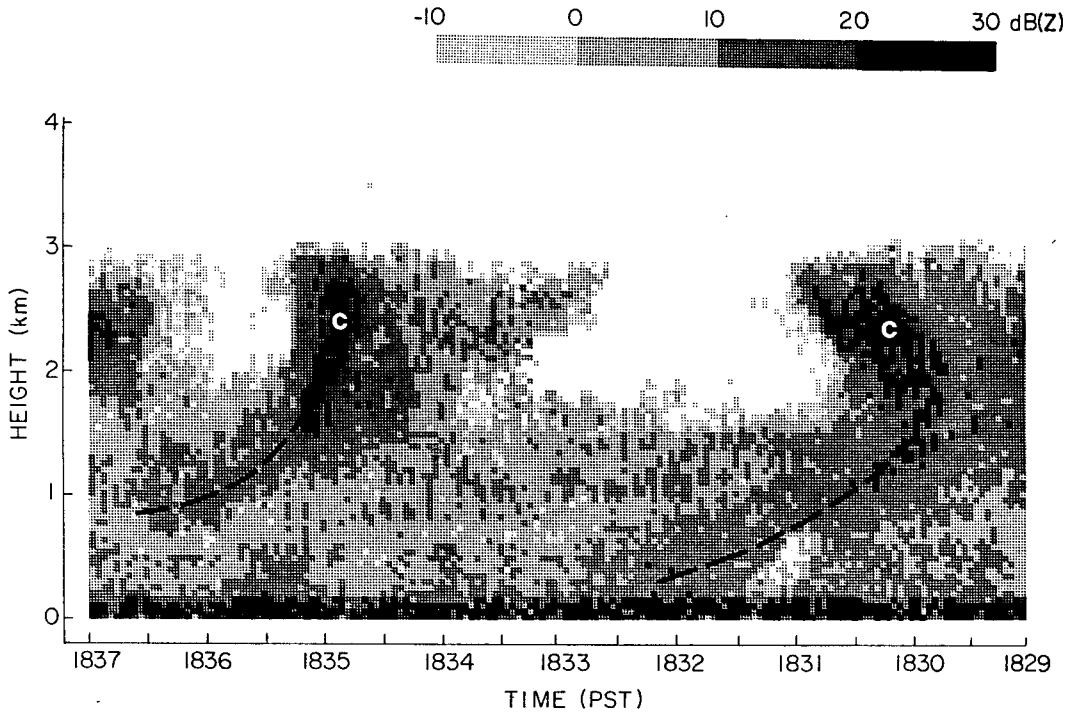

FIG. 13. Time–height cross section of the radar reflectivity measured with the 8.6 mm wavelength radar at Pt. Brown in rainband 1 of Case 2. The dashed lines indicated fallstreaks from the embedded, upper-level convection cells (**c**).

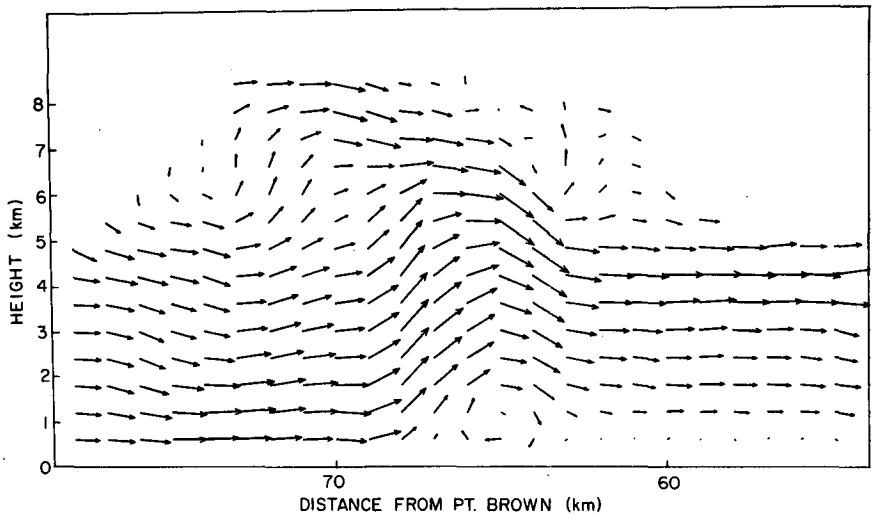

FIG. 14. Derived two-dimensional airflow (relative to the motion of the rainband) for rainband 4 in Case 1 at 0957 PST 17 January 1982.

Line AB in Fig. 17 is oriented perpendicular to rainband 2. Vertical cross sections through AB of the reflectivity, vertical velocity, and storm-relative airflow are shown in Fig. 18a–c, respectively. The flow field shows convergence near the middle of the cross section, toward the rear edge of the leading precipitation core, with relative inflow from the east at the leading edge of the band, becoming westerly behind the main convergence region. Again, it appears that cloud particles were carried aloft in this updraft, and then forward in the band where they fell out through the moist inflow at lower levels, resulting in the higher radar reflectivity forward of the main region of convergence. A secondary, weaker zone of convergence, associated with the precipitation core along the trailing half of the band, can be seen along the rear edge of the band. The vertical velocity pattern shows upward motions > 2 m s^{-1} above the region of strongest convergence, with a secondary zone of upward motion near the rear of the band. This is consistent with the airflow and reflectivity data.

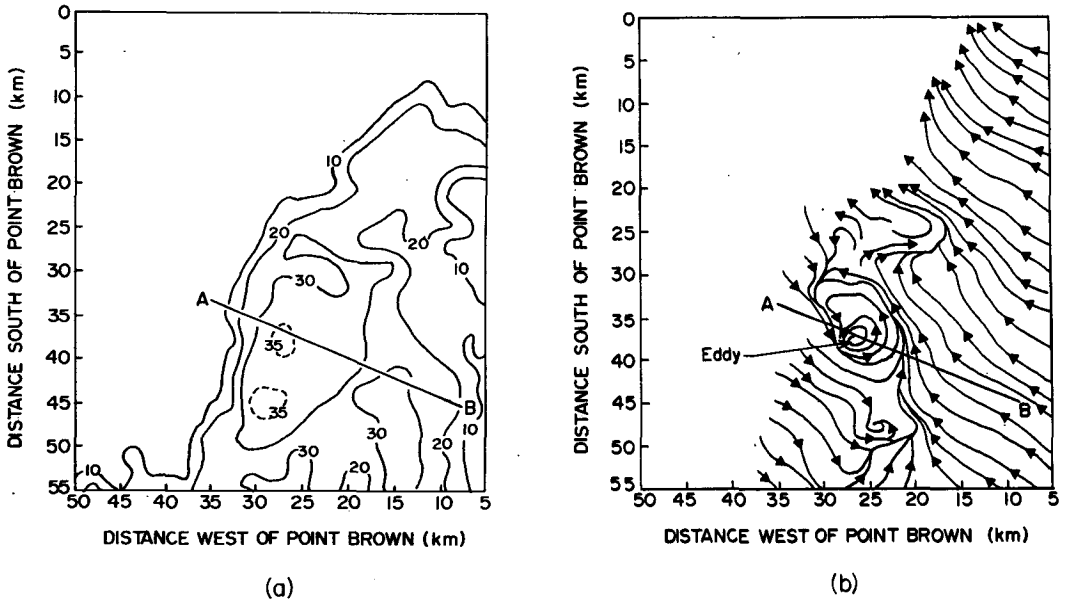

FIG. 15. Horizontal cross sections through rainband 1 in Case 2 at 1829 PST on 10 February 1982: (a) radar reflectivity (in dBZ) at 0.3 km altitude. (b) Streamlines of the airflow relative to the rainband at 0.9 km altitude. The arrow indicates the position of a mesoscale eddy. The line A–B indicates the orientation of the vertical cross section shown in Fig. 16.

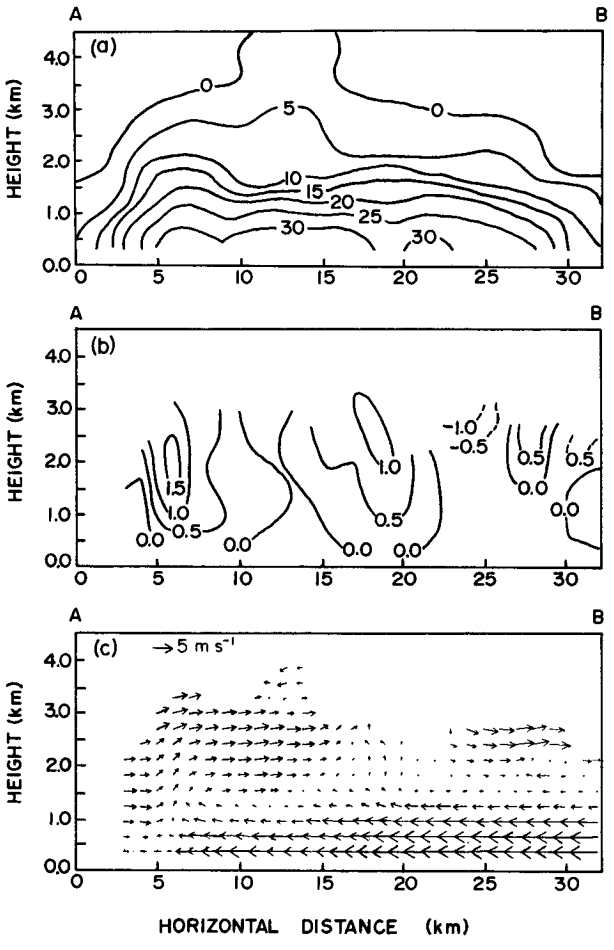

FIG. 16. Vertical cross sections along line A–B in Fig. 15 showing: (a) radar reflectivity (in dBZ), (b) vertical velocity (in m s^{-1}), and (c) airflow relative to the mean motion of the rainband.

7. Cloud microphysical structures

a. Case 1

Flight-level data were obtained from the NOAA P-3 aircraft from 1150 to 1530 PST 17 January 1982. However, aircraft data were obtained only after the rainbands were over the land. Rainband 4 contained regions with liquid water contents up to 1.6 g m^{-3} at 1 km, with a corresponding maximum in upward, vertical velocity of 2.7 m s^{-1} at that altitude. The maximum liquid water content decreased to 1.0 g m^{-3}, while the maximum upward vertical velocity measured from the P-3 was 4.4 m s^{-1} at 2.5 km altitude.

b. Case 2

In Case 2, extensive aircraft data was obtained from the University of Washington's B-23 aircraft, which flew a series of straight line paths across the width of rainband 2 (Fig. 12). Starting at an altitude of 4.5 km, the aircraft descended roughly 300 m at the end of each leg, before reentering the rainband.

The region of rainband 2 near cloud top was characterized by small updrafts, with maximum liquid water contents of ~0.5 g m^{-3}. The droplets were ≤ 25 μm in diameter and their concentrations $\leq$ 100 cm^{-3}. The updrafts formed in the unstable layer described in the previous section. The temperature near cloud top was −19°C, but few ice crystals (~0.03 L^{-1}) were detected there. Some small ice plates with radiating assemblages of side planes were apparent in the Particle Measuring System (PMS) 2D data. Increasing concentrations of ice crystals (up to 20 L^{-1}) were present in fallstreaks just below cloud top (3.5 to 4 km), with pristine dendrites appearing at the slightly higher temperatures in this layer.

The layer from 2.5–3.0 km in rainband 2 was near the top of the updraft that originated from convergence at low levels. This layer contained regions of pristine unrimed crystals, including dendrites and some aggregates (20–25 L^{-1}). The crystal habit indicates that the ice crystals were falling into this layer from aloft. In a shallow region of this layer, small, moderately rimed ice particles were encountered in concentrations up to 75 L^{-1}. In the region of rainband 2 near 1.5 km, which was near the level of strongest upward air motion (Fig. 16), there were large concentrations of rimed needles (up to 100 L^{-1}) and large (>5 mm) rimed aggregates.

Aircraft data from near the base (~0.7 km) of rainband 2 indicated the presence of a moderately strong updraft. At this level, the air temperature was about −0.4°C and the droplet concentration ~ 300 cm^{-3}. Large aggregates and a few ice needles were also present.

In summary, the aircraft data support the view that the rainbands contained active convective elements with significant liquid water contents and that these resulted from low-level convergence. In Case 2, small convective elements in the rainbands developed in an unstable layer near the top of the rainbands, and these elements provided ice crystals that grew by riming and aggregation as they descended.

8. Mechanisms for the rainbands

Parsons and Hobbs (1983) reviewed various dynamical mechanisms that might be responsible for the formation and maintenance of rainbands in extratropical cyclones. We now consider some of these mechanisms to see whether they can explain the rainbands in the comma clouds described in this paper.

a. Symmetric instability

Vertical cross sections of constant angular momentum and isotherms of wet-bulb potential temperature can be used to determine whether regions of the atmosphere are unstable to moist symmetric overturning (Emanuel, 1983). Matejka et al. (1980) found postfrontal rainbands to be aligned parallel to the thermal

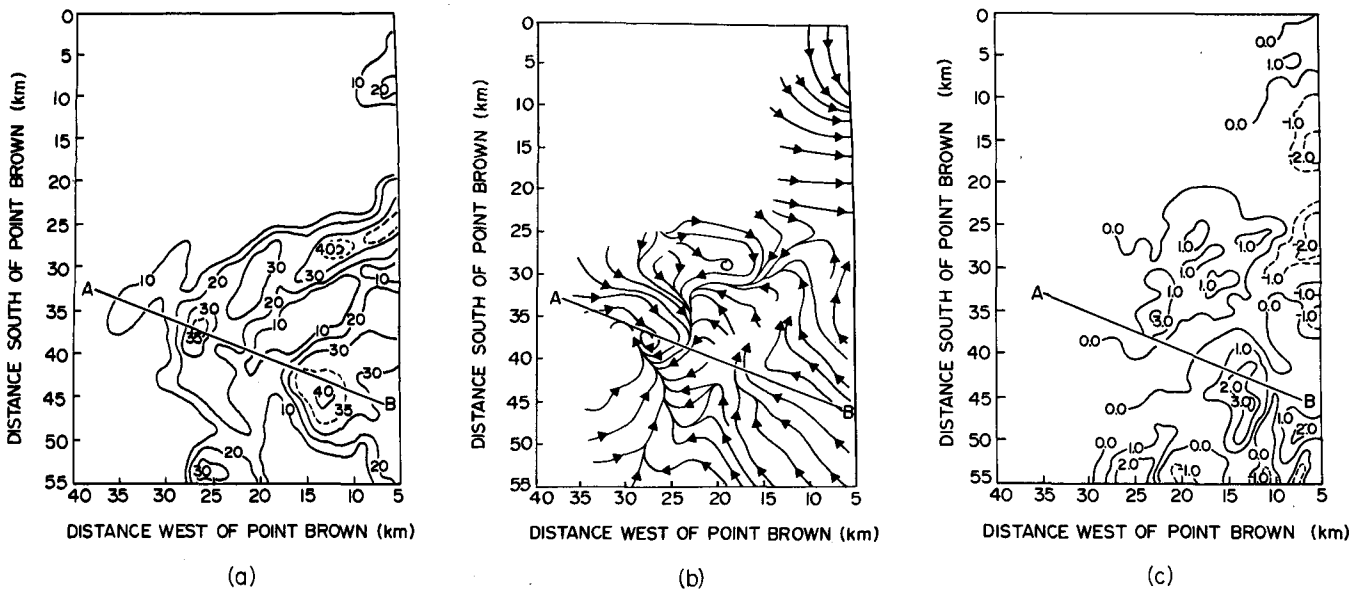

FIG. 17. Horizontal cross sections of rainband 2 in Case 2 at 2212 PST 10 February 1982: (a) radar reflectivity (in dBZ) at 0.3 km altitude. (b) Streamlines at 0.9 km altitude of the airflow relative to the rainband, and (c) vertical velocity (in m s^{-1}). The line A–B shows the orientation of the vertical cross section shown in Fig. 18.

wind and thus approximately along the vertical shear of the geostrophic wind, as predicted by symmetric instability theory. Seltzer et al. (1985) compared the characteristics of several rainbands located in midlatitude cyclones, although not associated with surface fronts. These rainbands were oriented parallel to the thermal wind, and may have been caused by symmetric instability. However, comparisons between theory and observations were hampered by the inability of the theory to account for ageostrophic shear and curved flow.

In some vigorous polar vortices, which may be strongly baroclinic in their lower levels, the criterion for symmetric instability may be met (M. Shapiro, personal communication). However, the baroclinicity in the rainbands described in this paper was small. Furthermore, the theory for symmetric instability predicts that the rainbands should be oriented parallel to the thermal wind in the overturning layer, whereas the thermal wind was perpendicular to the orientation of the rainbands. We conclude that symmetric instability was not responsible for the rainbands described in this paper.

b. Inflection-point instability

Rayleigh (1916) investigated the dynamic instability of sheared flows. He showed that local vorticity extremes are located at inflection points in plots of the horizontal wind with height (see, for example, Fig. 19b). At these points the fluid is unstable and the flow adjusts to remove this instability. In the planetary boundary layer, this can lead to the formation of rolls or waves, and, under certain conditions, rainbands (Brown, 1974, 1980). Inflection-point instability theory predicts the wavelength of the rolls to be about 2π times the height of the inflection point, and the motion of the rolls (perpendicular to their length) is predicted to be the same as the wind speed in that direction at the height of the inflection point.

To evaluate the applicability of the inflection-point instability theory to the rainbands discussed in this paper, the aircraft, rawinsonde and Doppler-radar data were used to construct profiles of the mean winds parallel and perpendicular to the orientation of the rainbands. The results for Case 1 are shown in Fig. 19. The propagation velocity of rolls predicted by inflection-point instability theory should be $\sim$23 m s^{-1}, whereas the propagation velocity was observed to be $\sim$7–8 m s^{-1} (Fig. 19a). It appears, therefore, that inflection-point instability was not responsible for these rainbands.

The measured profile of the mean winds along the length of the rainbands is shown in Fig. 19b. The exaggerated inflection in this component of the wind, which is seen at a height of $\sim$2.5 km, is characteristic of a profile that is conducive to the development of inflection-point instability. (The dashed curve in Fig. 19b is a hypothetical mean-wind profile of the undisturbed atmosphere.) However, since the inflection is in the wind component *along* the length of the rainbands, this mechanism can only explain variations in this direction. The height of the inflection point ($\sim$2.5 km) in the mean wind profile is almost the same as the height at which the vertical velocities in the precipitation cores reach their peak values. Also, the velocity ($\sim$11 m s^{-1}) of the precipitation cores along the rain-

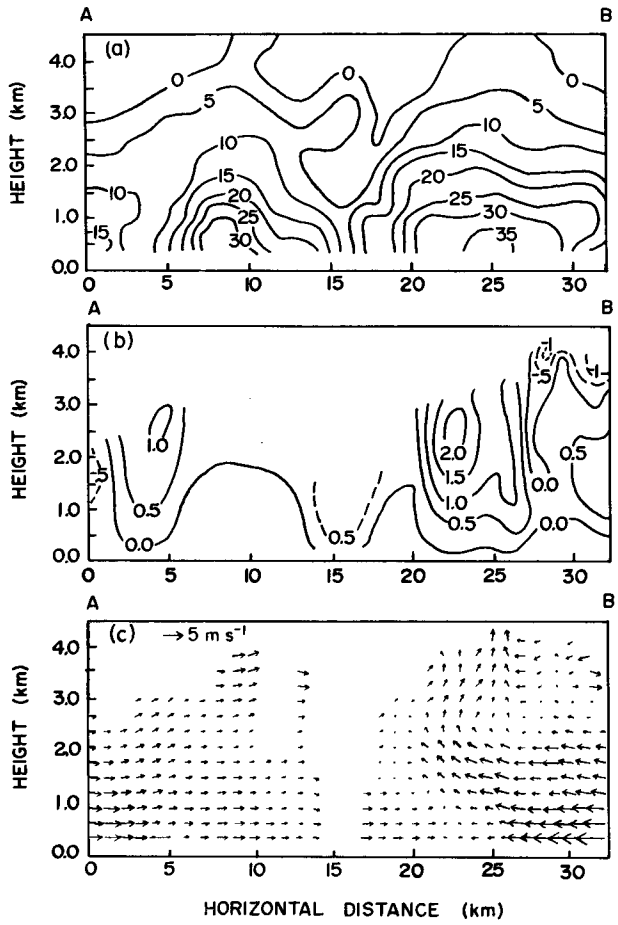

FIG. 18. Vertical cross sections, along the line A–B in Fig. 17, of (a) radar reflectivity (in dBZ), (b) vertical velocity (in m s^{-1}), and (c) airflow relative to the mean motion of the rainband.

band is about the same as the along-band phase velocity of the rolls at the height of the inflection point, as predicted by inflection-point instability theory. The predicted roll wavelength of ~16 km (~2π times the height of the inflection point) is consistent with the observed core spacing of 15–20 km.

The data from Case 2 yield results very similar to those for Case 1. Again, there is a strong inflection in the vertical profile of the component of the mean wind along the length of the rainbands (at a height of ~2.5 km), but a nearly linear shear in the wind components across the width of the rainbands.

It appears, therefore, that inflection-point instability theory cannot explain the formation of the rainbands themselves. However, the vertical profile of the mean winds along the length of the rainbands may have been modified by rolls or waves oriented perpendicular to the rainbands that resulted from an inflection-point instability. The velocities of the cores of precipitation embedded in the rainbands described in this paper are consistent with the wind velocity at the inflection point, as predicted by inflection-point instability theory. The precipitation cores may have formed in those regions where rolls, produced by inflection-point instability and aligned perpendicular to the length of the rainbands, crossed the rainbands and produced enhanced updrafts at the crossover points.

c. Internal gravity waves and dynamic/convective mechanisms

Recent numerical modeling results, using high-resolution, two-dimensional, nonhydrostatic models, show that when a divergent field is superimposed on a two-dimensional temperature gradient, gravity waves can produce a series of rainbandlike features in the vertical motion field, with wavelengths of ~25–50 km (Blumen, 1972; R. L. Gall, personal communication). Although Gall's model has a stable atmosphere, it is possible that a wave-CISK instability could provide a mechanism for the production of rainbands in cases where the large-scale dynamics causes the static stability of the atmosphere to decrease with time. However, this theory predicts the rainbands to be oriented parallel to the thermal wind, whereas the rainbands described in this paper were oriented perpendicular to the thermal wind.

Sun (1978) investigated the mesoscale organization of deep convective cloud lines through a linear-stability analysis that included the effects of moist-static stability, latent-heat release and wind shear. In treating the problem of convection in the tropics, Sun neglected the Coriolis force and limited his analysis to two ideal wind profiles: one with only speed shear with height and the other with a 90° turning of the wind with height (but no speed shear). Sun's results show that in regions where the buoyancy force released by latent heat is much stronger than the damping effect from static stratification, the rainbands will be aligned parallel to the wind shear vector ("longitudinal mode") in the layer of the rainbands and will be stationary with respect to the mean wind in the cloud layer; this minimizes the tendency of the shear to suppress the convection. Observations (Businger, 1986) show rainbands to be oriented parallel to the wind-shear vector when the mean-wind profile is dominated by cold advection (backing of the wind with height) and the air is conditionally unstable through most of the troposphere. However, in both of the case studies presented in this paper, the disturbances were dissipating as they passed through our observational network and the mean-wind profile was dominated by warm advection (veering of the wind with height) (Fig. 20a). Sun's (1978) results show that in cases where the buoyancy force is weak and the kinetic energy of the flow becomes dominant, rainbands should be oriented perpendicular to the wind shear and propagate relative to the mean flow ("transverse mode"). Figure 20a shows the shear of the mean wind over the depth of the rainbands for Case 2. It is

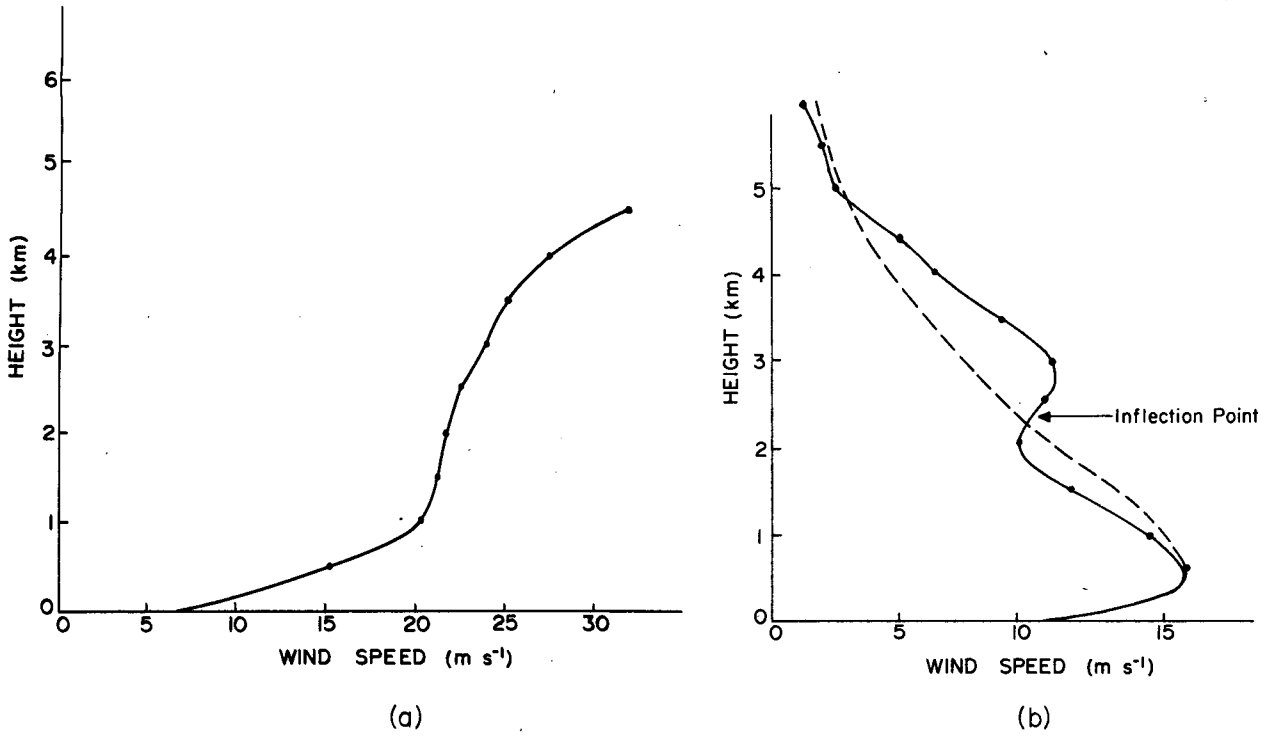

FIG. 19. Vertical profiles of the mean wind derived from rawinsonde and aircraft data for the rainbands in Case 1. (a) Wind component across the width of the rainband, and (b) wind component along the length of the rainband (solid curves). The dashed curve shows a hypothetical mean-wind profile prior to adjustment (from Fig. 9.2 in Brown, 1974).

interesting to compare this figure with Fig. 20b, taken from Sun (1978). In both cases, the rainbands are oriented with their lengths nearly perpendicular to the wind shear over the depth of the rainbands. Sun predicts the rainbands with a transverse mode to have a wavelength of ~50 km, which is very similar to the wavelength of the rainbands described in this paper. Although Sun's analysis was concerned with deep tropical convection, his results show that the transverse mode is dominant for shallower convection under drier conditions (such as those observed in polar air masses).

The observed phase speeds of the rainbands with respect to the mean flow were ~10 m s^{-1} for Case 1 and ~6 m s^{-1} for Case 2, which correspond to propagation frequencies of 1.3×10^{-3} s^{-1} and 7.5×10^{-4} s^{-1}, respectively. Sun's model predicts propagation frequencies for transverse-mode rainbands with cloud tops near 6 km to range from 1.3×10^{-3} s^{-1} to 2.5×10^{-5}

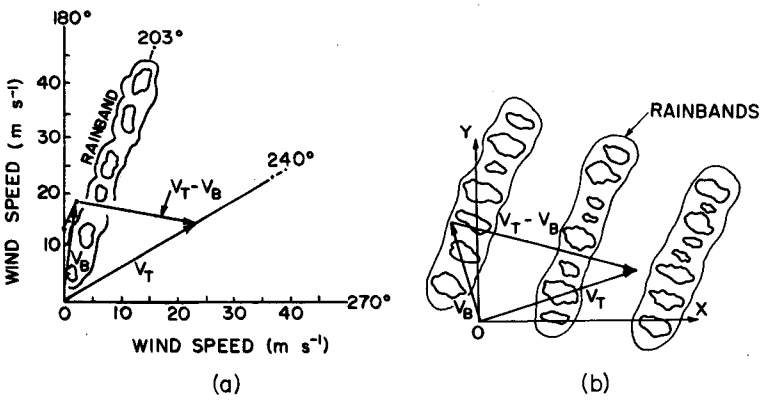

FIG. 20. (a) Orientation of the rainbands and the shear of the horizontal wind with height for Case 2. V_T and V_B are the wind velocities at cloud top and cloud base, respectively, and $V_T - V_B$ is the wind shear. Compare these observations with the predictions of Sun's (1978) theory, shown in (b), for the orientation of rainbands with respect to wind shear for the case of neutral stratification and a 90° shift in the wind direction with height.

s^{-1}. However, since the propagation frequencies and growth rates predicted by Sun's model are strongly dependent on the static stability, moisture supply and cloud depth, direct comparisons with observations should be made with caution.

It appears from the above discussion that the orientation and spacing of the rainbands discussed in this paper can be explained by the convective/dynamical model proposed by Sun (1978).

Sun (1984) used a linearized two-dimensional model to study the formation and evolution of rainbands in the warm sector of a midlatitude cyclone over the eastern United States. The results show that rainbands should propagate toward the warm side. Small weak bands are dissipated by subsidence warming associated with the downward motion of stronger adjacent rainbands, and, in their mature stage, they merge into a few large rainbands with horizontal wavelengths of a few hundred kilometers. Although these results apply to midlatitude cyclones, an analogous merging can be observed in strong comma clouds as they mature (see Fig. 2a and also Reed and Blier, 1986a,b).

9. Summary and conclusions

Satellite and synoptic data have been used to establish the large-scale environments in which two comma clouds occurred over the Pacific Ocean. Both disturbances formed in regions of moderately strong cyclonic vorticity and baroclinicity, with a surface low-pressure center coincident with the head of the comma cloud, and a surface-pressure trough situated under the trailing edge of the tail of the comma cloud. In both cases, there was a wind maximum near 850 mb, which was located on the southeast flank of the comma cloud just ahead of the short-wave trough. This feature is consistent with the presence of a tongue of warm air ahead of the trough and thermal wind balance.

Radar and satellite data revealed well-defined rainbands within both comma clouds. The average width of the rainbands was ~20 km and their average separation ~ 30 km (corresponding to a wavelength of ~50 km). The rainbands were aligned along the direction of the mean wind, and perpendicular to the thermal wind, within the depth of the rainbands. Precipitation cores within the rainbands (with a spacing along the rainbands of ~17 km) retained their identities and strengths over periods of several hours.

A schematic depiction of a rainband in a comma cloud is given in Fig. 21. This figure is a synthesis of the results of the mesoscale analyses of Doppler radar and aircraft data from the two case studies described in this paper. These results include the three-dimensional airflow relative to the rainband, showing the wind shift and line of convergence at low levels within

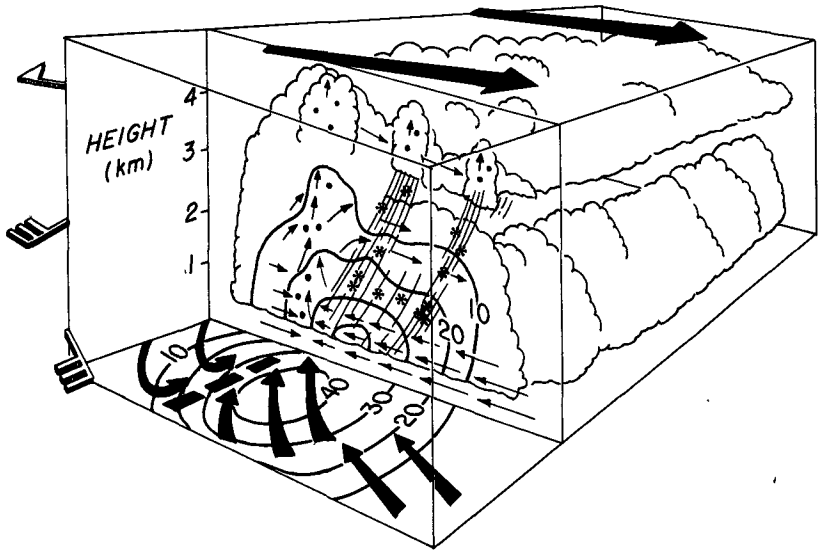

FIG. 21. Schematic depiction of a rainband in a comma cloud based on the information presented in this paper. The scalloped lines show the edge of the cloud. The front portion of the rainband has been omitted in order to show its microphysical structure in the vertical, the airflow relative to the band (heavy arrows), the convergence line (heavy dashed line) and radar reflectivity (solid contours marked in dBZ) just above the surface. The vertical cross section also shows the airflow relative to the band (small arrows) and radar reflectivity (solid contours marked in dBZ). Also depicted are small convective cells near the top of the rainband, from which fallstreaks emanate. The microphysical structure of the rainband is indicated by the solid dots (regions of relatively high liquid water content), and hexagons (regions of relatively high ice particle concentrations). Aggregates of ice particles are depicted by overlapping hexagons. On the left side of the figure, the change in wind speed with height is shown by the wind barbs (each barb equals 5 m s^{-1}, triangle equals 25 m s^{-1}). The wind direction just above the top of the rainband is shown by the large heavy arrows at the top of the figure.

the rainband. The convergence and associated updrafts were located along the rear edge of precipitation cores (indicated by high values of radar reflectivity in Fig. 21), with airflow from the west at the rear of the rainband, and at higher levels, spreading precipitation particles forward in the band where they fell out through a moist inflow from the east at low levels. Dual-Doppler radar data revealed vertical velocities of several meters per second, and aircraft measurements showed relatively high liquid water contents, indicating that the precipitation cores were the result of embedded convection. Also depicted in Fig. 21 are convective elements that formed in an unstable layer near the top of the rainband; these can produce ice crystals that grow by riming and aggregation in the lower moist levels, thereby enhancing precipitation.

The spacing of the rainbands and their orientation perpendicular to the thermal wind appear to be best explained by the theory for mixed dynamic/convective instability developed by Sun (1978). When buoyancy forces are weak, kinetic energy derived from the mean flow dominantes over buoyant energy. Under these conditions, rainbands can form with their lengths oriented perpendicular to the thermal wind vector, and with a wavelength of ~50 km, similar to the rainbands described in this paper. It is possible that rolls produced by inflection-point instability, and aligned nearly perpendicular to the length of the rainbands, produced enhanced updrafts where they intersected the rainbands, thereby resulting in embedded cores of precipitation at these locations.

Acknowledgments. We wish to thank all members of the University of Washington's Cloud and Aerosol Research Group who helped in this research. The two scanning-Doppler radars (CP-3 and CP-4) were provided and operated by the Field Observing Facility of NCAR, and the P-3 aircraft was operated by NOAA. We are grateful to the personnel from both of these organizations for their considerable help in gathering data. The Scientific Computing Division of NCAR provided computing resources.

This research was supported by the Division of Atmospheric Sciences, National Science Foundation, under Grant ATM-8306132, and by the Naval Air Systems Command through ONR Contract N00014-86-C-2246.

REFERENCES

Anderson, R. K., J. P. Ashman, F. Bittner, G. R. Farr, E. W. Ferguson, V. J. Oliver and A. H. Smith, 1969: Application of meteorological satellite data in analysis and forecasting. ESSA Tech. Rep. NESC 51, U.S. Dept. of Commerce, Washington, DC. [NTIS Number AD-697 022].

Blumen, W., 1972: Geostrophic adjustment. *Rev. Geophys. Space Phys.*, **10,** 485–528.

Brown, R. A., 1974: *Analytical Methods in Planetary Boundary Layer Modeling.* Wiley and Sons, 150 pp.

——, 1980: Longitudinal instabilities and secondary flows in the planetary boundary layer: a review. *Rev. Geophys. Space Phys.*, **18,** 683–697.

Businger, S. A., 1985: The synoptic climatology of polar low outbreaks. *Tellus,* **37A,** 419–432.

——, 1986: Cyclonic vortices in polar air masses. Ph.D. thesis, University of Washington.

Emanuel, K. A., 1983: On assessing local conditional symmetric instability from atmospheric soundings. *Mon. Wea. Rev.*, **111,** 2016–2033.

Forbes, G. S., and W. D. Lottes, 1985: Classification of mesoscale vortices in polar airstreams and the influence of the large-scale environment on their evolution. *Tellus,* **37A,** 132–155.

Harrold, T. W., and K. A. Browning, 1969: The polar low as a baroclinic disturbance. *Quart. J. Roy. Meteor. Soc.* **95,** 710–723.

Hobbs, P. V., 1978: Organization and structure of clouds and precipitation on the mesoscale and microscale in cyclonic storms. *Rev. Geophys. Space Phys.*, **16,** 741–755.

——, T. J. Matejka, P. H. Herzegh, J. D. Locatelli and R. A. Houze Jr., 1980: The mesoscale and microscale structure and organization of clouds and precipitation in midlatitude cyclones. I: A case study of a cold front. *J. Atmos. Sci.*, **37,** 568–596.

Locatelli, J. D., P. V. Hobbs and J. A. Werth, 1982: Mesoscale structures of vortices in polar air streams. *Mon. Wea. Rev.*, **110,** 1417–1433.

Matejka, T. J., R. A. Houze, Jr. and P. V. Hobbs, 1980: Microphysics and dyanmics of clouds associated with mesoscale rainbands in extratropical cyclones. *Quart. J. Roy. Meteor. Soc.*, **106,** 29–50.

Mayengon, R., 1983: Warm-core cyclones in the Mediterranean. *Mariner's Wea. Log.*, **28,** 6–9.

Parsons, D. B., and P. V. Hobbs, 1983: The mesoscale and microscale structure and organization of clouds and precipitation in midlatitude cyclones. XI: Comparisons between observational and theoretical aspects of rainbands. *J. Atmos. Sci.*, **40,** 2377–2397.

Rasmussen, E., 1979: The polar low as an extratropical CISK disturbance. *Quart. J. Meteor. Soc.*, **105,** 531–549.

——, 1981: An investigation of a polar low with a spiral cloud structure. *J. Atmos. Sci.*, **38,** 1785–1792.

——, 1983: A review of mesoscale disturbances in cold air masses. *Mesoscale Meteorology—Theories, Observations, and Models.* D. K. Lilly and T. Gal-Chen, Eds., Reidel, pp. 247–283.

——, 1985: A case study of a polar low development over the Barents Sea. *Tellus,* **37A,** 407–418.

Rayleigh, Lord, 1916: On convection currents in a horizontal layer of fluid when the higher temperature is on the underside. *Phil. Mag.*, **32,** 529–546.

Reed, R. J., 1979: Cyclogenesis in polar airstreams. *Mon. Wea. Rev.*, **107,** 38–52.

——, and W. Blier, 1986a: A case study of comma cloud development in the eastern Pacific. *Mon. Wea. Rev.*, **114,** 1681–1695.

——, and ——, 1986b: A further case study of comma cloud development in the eastern Pacific. *Mon. Wea. Rev.*, **114,** 1696–1708.

Seltzer, M. A., R. E. Passarelli and K. A. Emanuel, 1985: The possible role of symmetric instability in the formation of precipitation bands. *J. Atmos. Sci.*, **42,** 2207–2219.

Sun, W.-Y., 1978: Stability analysis of deep cloud streets. *J. Atmos. Sci.*, **35,** 466–483.

——, 1984: Rainbands and symmetric instability. *J. Atmos. Sci.*, **41,** 3412–3426.

Wang, P.-Y., and P. V. Hobbs, 1983: The mesoscale and microscale structure and organization of clouds and precipitation in midlatitude cyclones. X: Wavelike rainbands in an occlusion. *J. Atmos. Sci.*, **40,** 1950–1964.

Wilhelmsen, K., 1981: The polar low near the Norwegian coast. Tech. Rep. No. 55, Det Norske Meteorologiske Institutt, 33 pp. [Available from Norsk Meteor Institutt, Vervarslinga for Nord-Norge, P.O. Box 2760, Elverhoy, 9001, Tromso, Norway.]

World Meteorological Organization, 1973: The use of satellite pictures in weather analysis and forecasting. Tech. Note 124, 275 pp. [Available from WMO, 41 Giuseppe-Motto, Case postale No. 5, CH-1211, Geneva 20, Switzerland.]

Zick, C., 1983: Method and results of an analysis of comma cloud developments by means of vorticity fields from upper tropospheric satellite wind data. *Meteor. Rdsch.*, **36,** 69–84.